Al-Nahrain Journal for Engineering Sciences

Al-Nahrain J. Eng. Sci. 29(2) 291-300, 2026
Original Article

Functionally Graded Materials of Stainless Steel 316L-Inconel 625: Optimization of the study characteristics through Porosity, Microstructure, and Mechanical Performance

Samir Noori Ali [1]●, Ziad Aeyad Taha [2]● and Barbara Previtali [3]●.

1,2Institute of Laser for Postgraduate Studies, University of Baghdad, Baghdad, Iraq
3Department of Mechanical Engineering, Politecnico di Milano, Via La Masa 1, 20156 Milan, Italy

●*These authors contributed equally to this work*

DOI: https://www.doi.org/10.29194/NJES.29020291

Received: Jan. 21, 2026 **Revised:** Feb. 26, 2026 **Accepted:** March 17 2026 **Published:** June 20, 2026

Abstract

Functionally graded materials were created using laser-directed energy deposition technology. This work examines how different mixing ratios of Stainless Steel 316L and Inconel 625 affect the relative density and porosity of these materials. Twelve samples were created using a constant laser power of 600 W, three different laser scan speeds (20, 25, and 30 mm/s), and four different SS316L/IN625 transition ratios (85%/15%, 60%/40%, 40%/60%, and 15%/85%). To determine the volumetric distribution across the compositional gradients, the porosity and relative density measurements were taken. Optical and scanning electron microscopy were used for microstructural analytical characterization to differentiate between compositional gradients in grain shape and phase distribution. The mechanical performance was examined using microhardness measures, namely the Vickers method. This study applied to prove the process parameters and compositional transformations to the resulting microstructural features and mechanical properties, providing insight into optimizing the laser-directed energy deposition-manufactured functionally graded materials for advanced performance. The best graded composition was found that gives the best overall performance based on experimental data.

Keywords: *Additive Manufacturing, Laser Directed Energy Deposition (LDED) technique, Gradient Metallurgy, Functionally Graded Material (FGM), SS316L/IN625 alloys, Microstructural Texture Evolution.*

Corresponding author: Provide the corresponding author information and publisher here. E-mail address: samirnoori@ilps.uobaghdad.edu.iq

1. Introduction

Functionally graded materials (FGMs) represent an advanced class of engineered composites in which chemical composition and microstructure are intentionally varied—either continuously or discretely—across the component volume. This spatial variation enables localized control of mechanical, thermal, and corrosion-related properties beyond those achievable in homogeneous alloys [1].

In the present study, stainless steel 316L (SS316L) and the nickel-based superalloy Inconel 625 (IN625) were combined to exploit their complementary characteristics: SS316L is characterized by good ductility, formability, and economic efficiency, whereas IN625 exhibits superior high-temperature strength and corrosion resistance [2]. The integration of these alloys within a graded architecture provides a model system for investigating compositional transition effects in dissimilar metallic systems [3]. Such graded configurations have been examined in previous studies for components exposed to combined mechanical and environmental loading [4].

Laser-directed energy deposition (LDED) is particularly suitable for fabricating FGMs due to its capability for in situ multi-powder feeding and controlled energy input [5]. By independently adjusting powder feed ratios and scan parameters, LDED enables systematic modulation of thermal gradients, melt pool geometry, dilution behavior, and solidification kinetics. This process flexibility facilitates controlled formation of graded microstructures through compositional mixing within a common melt pool [6].

Porosity is a recurrent defect in graded metallic systems, typically appearing as sub-spherical gas pores or irregular interdendritic cavities. These defects originate from incomplete fusion, gas entrapment, melt pool instability, or powder-related irregularities. Consequently, careful optimization of processing parameters is required to minimize porosity and maintain microstructural continuity across compositional transitions [7]. Spatially controlled multi-material additive manufacturing, in which distinct materials are deposited within a single build, provides a platform for investigating localized property gradients under controlled processing conditions [8].

Zhong et al. [9] investigated melt pool behavior in nickel-based alloys during high-speed laser metal deposition and demonstrated that variations in thermal convection significantly influence solidification dynamics and gas evolution. Chen et al. [10] reported that increasing

IN625 content enlarges primary dendrite arm spacing and promotes precipitation of secondary phases at high alloy fractions, with corresponding changes in hardness. Ferreira et al. [11] observed a continuous hardness transition across graded regions and highlighted the influence of thermal history on heat-affected zone dimensions. Ghanavati et al. [12] showed that repeated remelting and heat accumulation during multilayer deposition modify microstructural scale and segregation behavior, leading to measurable variations in local hardness. Jones et al. [13] examined SS304–IN625 joints and demonstrated that compositional balance strongly influences interfacial integrity and cracking susceptibility. Hotz et al. [14] produced graded metallic systems via LDED and emphasized that gradual compositional transitions mitigate interfacial brittleness. Gotoh et al. [15] demonstrated that power density is a dominant factor governing porosity formation in laser-based additive manufacturing processes.

Guanyu Jiang et al. [16] evaluated the corrosion behavior of IN625 and SS316L under supercritical water conditions and reported distinct degradation mechanisms associated with alloy chemistry and environmental composition, highlighting the importance of understanding compositional effects in multi-material systems.

In this study, SS316L–IN625 graded alloys were fabricated using LDED and characterized in terms of porosity, microstructure, relative density, and microhardness to establish quantitative process–structure–property relationships within the investigated parameter range. Powder mixing ratio and scanning speed were systematically varied to evaluate their influence on compositional transition stability and defect formation. The experimental results indicate that a gradient composition of 40 wt.% SS316L–60 wt.% IN625 provides the lowest measured porosity, improved microstructural continuity across the transition zone, and higher hardness relative to the other investigated ratios. These findings are restricted to the defined processing conditions and provide an experimentally supported basis for understanding compositional grading effects in SS316L–IN625 systems.

2. Experiment

In this research, two types of powdered alloys were used, namely stainless steel 316L (SS316L) and nickel-based superalloy Inconel 625 (IN625). The particle sizes of the SS316L powder ranged from 56 to 100 µm, while those of the Inconel 625 powder ranged from 55 to 115 µm, as shown in Figs. 1 and 2, respectively. Also, the volumetric distribution was illustrated in Figs. 3 and 4. The chemical compositions of both powders are detailed in Tables 1 and 2.

Table 1. Chemical Composition of SS316L

El.	C%	Cr%	Mn%	Mo%	P%	Si%	Ni%	Fe%
Co	0.03	19.09	1.14	2.32	0.5	0.71	10.07	balance

Table 2. Chemical Composition of IN625

El.	Fe %	Ti%	Cr%	Al%	Mo%	Nb %	Si%	Ni%
Co	1.1	0.32	22.2	0.66	9.05	3.75	0.71	balanc

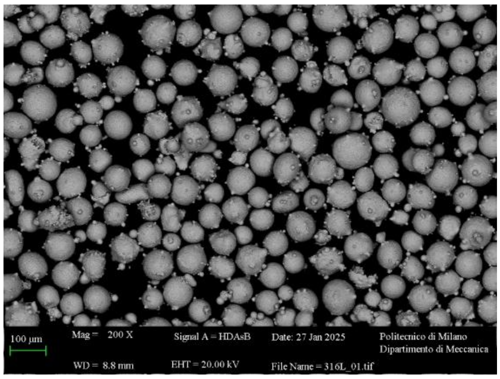

Figure 1. SEM of SS316L powder

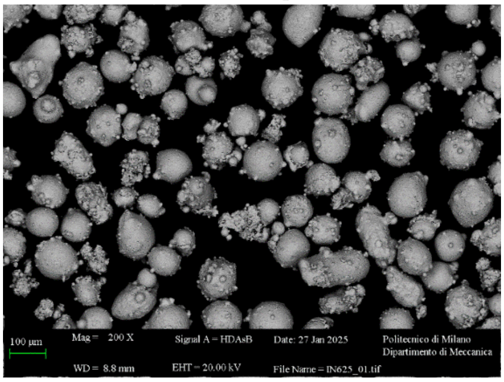

Figure 2. SEM of IN625 powder

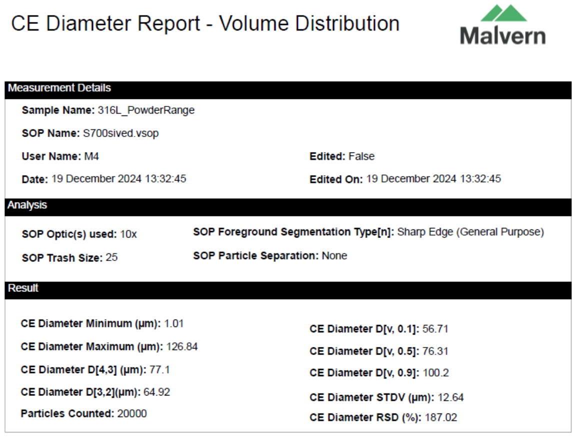

Figure 3. Volume distribution of SS316L

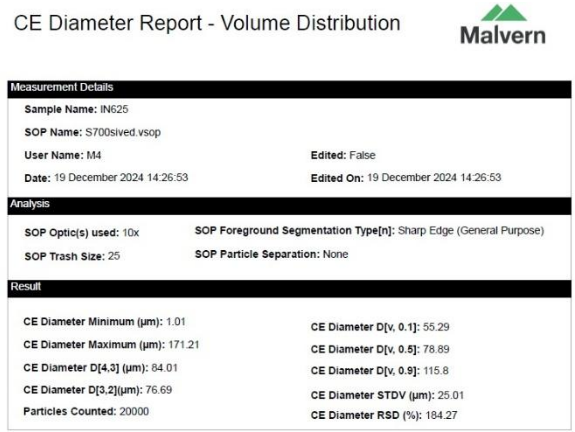

Figure 4. Volume distribution of IN625

In this case study, an IPG YLS-3000 3 kW ytterbium-doped fiber laser operating at a wavelength of 1070 nm (±10 nm) with a Gaussian beam intensity distribution was used, as shown in Fig. 5. producing a laser spot diameter of 1.2 mm at the focal point. The system was integrated with an ABB industrial robotic arm coupled with a circular two-axis table, enabling precise multi-axis motion control and flexible deposition strategies. Argon gas was used as the shielding and carrier gas during the laser deposition process. A raster scanning strategy was applied to deposit successive 0.2 mm thickness for each track layer by zigzag for cubes building strategy to form metal parts with a total height of 12 mm (each section was 4 mm in height as shown in Fig. 6).

Figure 5. Ytterbium fiber laser and LDED printhead.

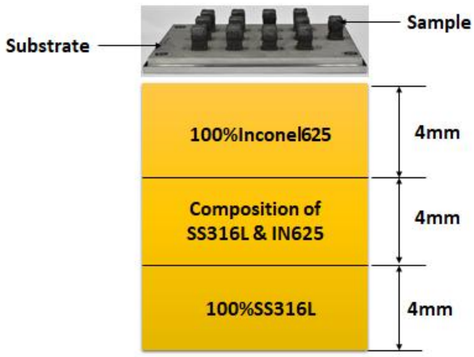

Figure (6) Layered Structure of FGM Sample: SS316L–IN625 with Graded Composition

The powder material was introduced into the melting bath via a coaxial nozzle using a GTV TWIN PF 2/2 powder feeder, ensuring high precision at a feed rate of 0.01 rpm, enabling stable and robust powder flow. Which means the feeder delivered powder by extremely slow, precisely metered rotations of the dosing screw/roller. The account of study at a low rotational speed gives very fine volumetric control of the powder stream and reduces transient pores, so the powder flow into the melt pool is stable and reproducible—provided the feeder has been calibrated for the specific powder morphology and bulk density [17]. The system includes two individual hoppers, each one for feeding SS316L and IN625 powders in separate modes, as shown in Figure 7.

The key process parameters include a laser power fixed at 600 watts, scanning speeds of 20, 25, and 30 mm/s, and a combined powder flow rate of 9.5 g/min for both powders. Argon gas was supplied at a flow rate of 25 L/min for protection and 7.5 L/min for powder delivery. The nozzle-to-substrate distance (standoff distance) was maintained at 12 mm. The used overlap of 50%, and hatch spacing of 0.6 mm, which is typical for LDED processes and ensures sufficient melt pool overlap for good metallurgical bonding.

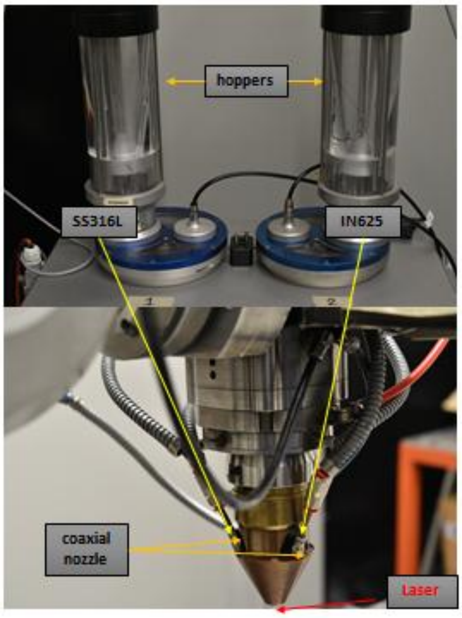

Figure (7) Dual-Hopper LDED Setup with Coaxial Nozzle and IPG YLS-3000 Laser Head

Functionally graded samples were fabricated with the following layered structure: a 4 mm height base of 100% SS316L, a 4 mm height middle zone containing graded compositions (85%/15%, 60%/40%, 40%/60%, and 15%/85% SS316L to IN625 ratios), and a 4 mm height top layer of 100% IN625. The substrate material used was 304L stainless steel, measuring 120 mm × 100 mm × 6 mm. Fig. 8 shows Cross-sectional macrograph of the SS316L–IN625 functionally graded structure fabricated by LDED, distinguishing the distinct regions of 100% SS316L (4 mm), composition transition zone (4 mm), 100% IN625 (4 mm), and the SS304L substrate. The details of SS304L chemical composition in Table 3. All other fixed parameters for the LDED process was reported in Table 4.

Table 3. Parameters

Element	C%	Si %	Mn %	Ni %	Cr %	P%	S%	Fe%
Continent	0.03	0.75	2	12	20	0.045	0.03	balance

Table 4. Fixed LDED Process Parameters

Category	Parameter	Value
Energy Input Control	Laser power	600 W
	Spot size	1.2 mm
	Standoff Distance (SOD)	12 mm
Material Delivery	Total Powder Flow Rate	9.5 g/min
Layer Formation	Layer thickness	0.2 mm
	Hatch Spacing	0.6 mm
	Overlap	50%
Shielding and Process Atmosphere	Carrier Gas	7.5 L/min
	Shielding Gas	25 L/min

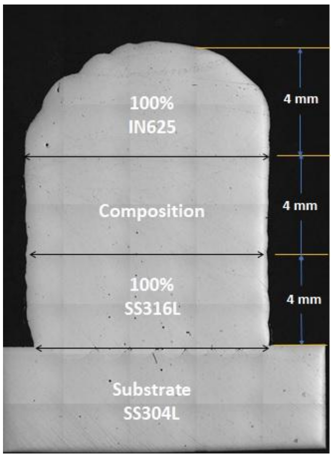

Figure 8. Cross-section of the SS316L–IN625 graded build highlighting substrate, SS316L, transition, and IN625 regions.

The dimensions of the final workpiece were 10 mm × 10 mm × 12 mm. The metallographically prepared samples were chemically etched using aqua regia, consisting of nitric acid and hydrochloric acid mixed in a 1:3 volume ratio (HNO_3: HCl), to effectively reveal the microstructural features of the SS316L–IN625 composition, following recent practices reported for laser-deposited multi-material systems. The density of the functionally graded sample was detected through a Mitutoyo Quick Vision Pro optical coordinate measuring instrument.

Quantitative porosity analysis was performed using ImageJ software. Optical micrographs acquired from polished and etched cross-sections were used for analysis. For each sample, multiple images were captured at identical magnification from representative regions across the deposited area to ensure statistical reliability. The images were first converted to grayscale and subjected to contrast enhancement to improve pore–matrix differentiation. A global thresholding method was applied to segment pores from the metallic matrix, followed by manual verification to remove artifacts and non-relevant features. Porosity was quantified by calculating the ratio of the total pore area to the total analyzed area. The reported porosity values represent the average of all analyzed images for each processing condition.

Optical microscopy (OM) and scanning electron microscopy (SEM) were employed to systematically analyze and clearly reveal the microstructural characteristics of the SS316L–IN625 composition. OM was used to examine the overall solidification morphology, melt pool features, and track-to-track and layer-to-layer characteristics across the deposited region, while SEM provided higher-resolution observation of the cellular and dendritic substructures, pore morphology, and microstructural heterogeneity at the microscale. The combined use of OM and SEM enabled a comprehensive interpretation of microstructural evolution arising from the laser deposition process and the interaction between the SS316L and IN625 constituents. Mechanical performance was calculated through Vickers microhardness testing, which was performed using a load of 300 g and a dwell time of 10 s, enabling assessment of local property variations caused by microstructural evolution and porosity distribution.

Hardness profiles (Fig. 9 [18]) were obtained along three vertical traverses across the cross-section (edge–center–edge) from the substrate interface to the top of the deposited height. A total of 180 independent indentations were conducted, consisting of 60 measurements along each traverse. A minimum center-to-center spacing of at least three times the indentation diagonal length was maintained between adjacent indents to avoid interaction effects, in accordance with ASTM E384. The hardness values obtained from each traverse were subsequently averaged, and the mean values were used for plotting and comparative analysis.

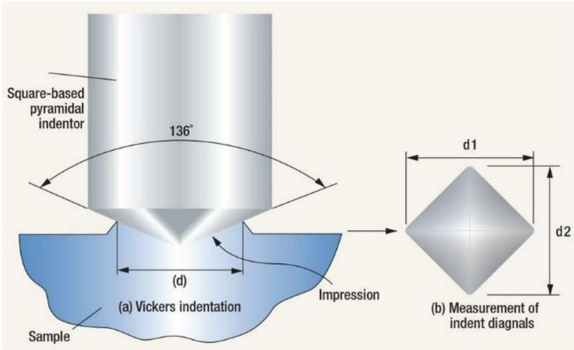

Figure 9. Principal of Hardness Vickers Calculation [18].

3. Results and discussion

3.1. Microstructure

Using OM and SEM, a systematic analysis was conducted on the microscopic detection of FGMs in SS316L-IN625 gradient samples. Twelve samples were generated in this study using a constant 600 W laser power. Scan speeds of 20, 25, and 30 mm/s and composition gradients of 85%/15%, 60%/40%, 40%/60%, and 15%/85% for the SS316L-IN625 metal powders were the primary factors in this case. The core graded section of each mixed sample was 4-mm thick. Variations in microstructure were significantly affected by changes in travel speed and component percentage. The samples were mechanically ground and polished to standard specifications before being chemically treated with appropriate chemicals to expose the crystalline/dendritic structure and microstructure of the melted zone.

When transitioning from regions rich in 316L stainless steel to regions rich in nickel as a balance contained in IN 625, the microstructure changes from a fine-grained austenitic structure to a coarser, more dendritic structure with increased spacing between the dendrites [19]. The primary dependencies are the linear energy density (J/mm) and scan speed (mm/s) at a constant input power (W). The mixed-phase structures exhibit microstructure variations at two levels: (1) the level of molten pool geometry, which is influenced by geometric dimensions and process parameters, and (2) the level of micro-segregation, which is characterized by the accumulation of niobium and molybdenum in the nickel-rich regions [20]. Optimizing the deposition process (increasing energy per unit length at a given energy-to-scan-speed ratio) reduces microstructure inhomogeneity, resulting in a more uniform appearance with fewer visible interfaces and lower porosity [21]. For 85%/15%, there are three different speeds: 20 mm/s Fig. 10(a), high heat input/low cooling rate: coarse austenitic matrix with coarse primary dendrites, large Secondary Dendrite Arm Spacing (SDAS), enhanced interdendritic segregation, and tendency toward columnar growth and grain coarsening. 25 mm/s Fig. 11(a); intermediate heat input:

mixed cellular-dendritic structure, reduced SDAS vs 20 mm/s, partial refinement of interdendritic segregation, and smaller epitaxial grains. 30 mm/s Fig. 12(a); low heat input/high cooling rate: fine cellular/dendritic microstructure, minimal segregation, highest homogenization, and hardness among SS316L-rich conditions. At 60%/40%: 20 mm/s Fig. 10(b); high heat input: coarsened primary/secondary dendrites, stronger Ni/Cr/Mo segregation in interdendritic regions, and increased risk of Laves-type interdendritic phases; pronounced columnar growth. 25 mm/s Fig. 11(b); intermediate: finer dendrites than 20 mm/s, reduced interdendritic Laves segregation, mixed cellular-dendritic morphology, and improved microstructural continuity. 30 mm/s Figures 12(b); high cooling rate, refined cellular dendrites, suppressed coarse interdendritic Laves, more homogeneous matrix, higher hardness, and finer precipitate distribution. At 40%/60%: 20 mm/s Fig. 10(c); high heat input: coarse dendritic Ni-rich matrix, strong interdendritic segregation, and larger solute-rich eutectic/Laves regions; coarsened γ'/Laves precursors and columnar grains. 25 mm/s Fig. 11(c): intermediate: partial refinement of dendrite arms, reduced solute banding, fewer continuous Laves networks, and improved ductile matrix continuity. 30 mm/s Fig. 12(c); high cooling rate, very fine cellular/dendritic Ni-rich structure, minimal interdendritic Laves formation, best homogenization, and fine precipitate dispersion (highest strength/lowest segregation). At 15%/85%: 20 mm/s Fig. 10(d); high heat input: very coarse Ni-rich dendrites with strong interdendritic segregation and continuous Laves/eutectic films; large columnar grains and reduced toughness. 25 mm/s Fig. 11(d); intermediate: reduced SDAS and partial breakup of interdendritic Laves, improved matrix continuity but still Ni-rich coarser morphology. 30 mm/s Fig. 12(d); high cooling rate, fine Ni-rich cellular structure, greatly decreased interdendritic Laves/eutectic, refined precipitates, and increased hardness/strength.

The sample fabricated from a 40% SS316L - 60% IN625 alloy, using a scanning speed of 30 mm/s (linear energy density of 20 J/mm, power of 600 W), exhibited the best microstructure and overall mechanical properties.

The optimum microstructural condition is proved when it provides the most stable and continuous transition across the graded region under the investigated processing parameters. At this ratio, the solidification morphology exhibits a uniform cellular-dendritic structure with reduced heterogeneity, indicating balanced dilution and controlled melt pool mixing between the Fe-based and Ni-based matrices. The transition zone does not display abrupt morphological discontinuities, excessive segregation contrast, or pronounced defect clustering, suggesting improved metallurgical compatibility and thermal stability during deposition. In addition, the mechanical response across the gradient shows a clearer and smoother hardness evolution from SS316L to IN625, reflecting compositional uniformity and microstructural consistency. Collectively, this ratio represents a thermally and chemically balanced state in which densification, microstructural continuity, and local mechanical response are simultaneously optimized within the defined experimental window.

These characteristics explain the low porosity and relatively high density compared to other samples. Furthermore, the improved wettability and reduced surface tension of the molten metal in this composition contributed to minimizing defects and gas entrapment, while rapid solidification reduced solute segregation, maintaining the integrity of the intergranular phases instead of forming a network, thus increasing strength while maintaining ductility. Therefore, the 40% SS316L-60% IN625 composition at a scanning speed of 30 mm/s was the optimal choice in this study.

On the other hand, SEM results confirm the OM findings, showing a finer microstructure in the samples fabricated with a 40% SS316L and 60% IN 625 alloy composition at a scanning speed of 30 mm/s and a laser power of 600 W, compared to other samples. Based on SEM, the microstructure characteristic is uniform, with small number of grains and precipitates that form between the grains instead of layers of precipitates. Cross-sectional images from SEM detection. Also show that there are no large voids caused by incomplete fusion and only small, round pores.

The visible microstructural features in the scanning electron micrographs explain why the samples have great mechanical properties, low porosity in particular mixing, and high relative density without being brittle. A high scanning speed which produced of El = 20 J/mm, the cooling process is increased, makes the grain structure more even, and prevents solute precipitation. A chemical composition of 40% SS316L-60% IN625 makes the molten metal surface more wett-able and reduces thermal stress. These factors totally contribute to minimizing defects and improving mechanical performance. Therefore, the SEM results confirm the OM findings.

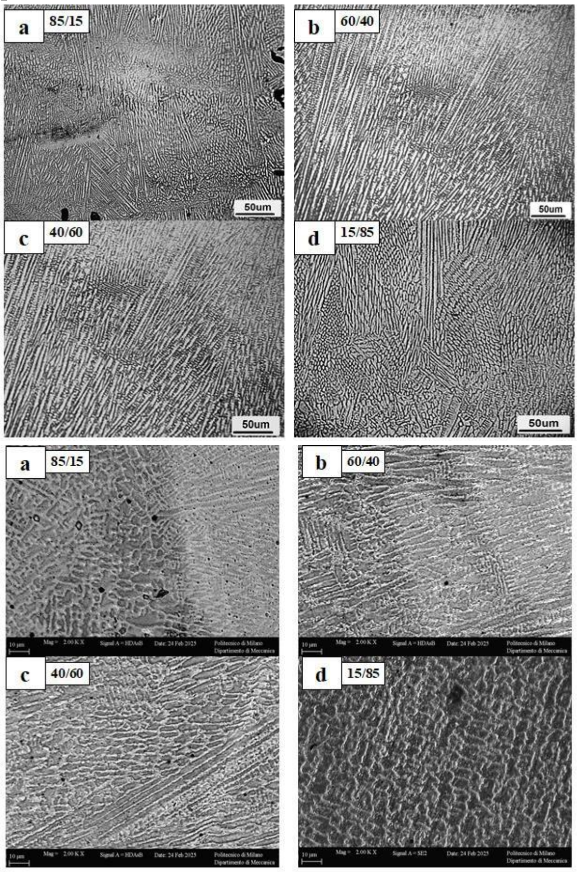

Figure 10. OM and SEM images of the composition region at different mixing ratio at v=20 mm/s.

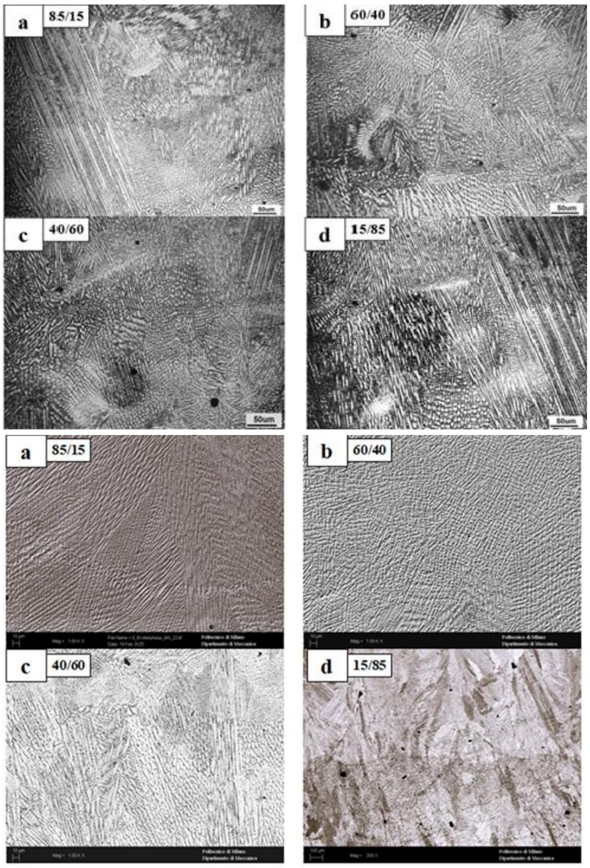

Figure 11. OM and SEM images of the composition region at different mixing ratio at v=25 mm/s.

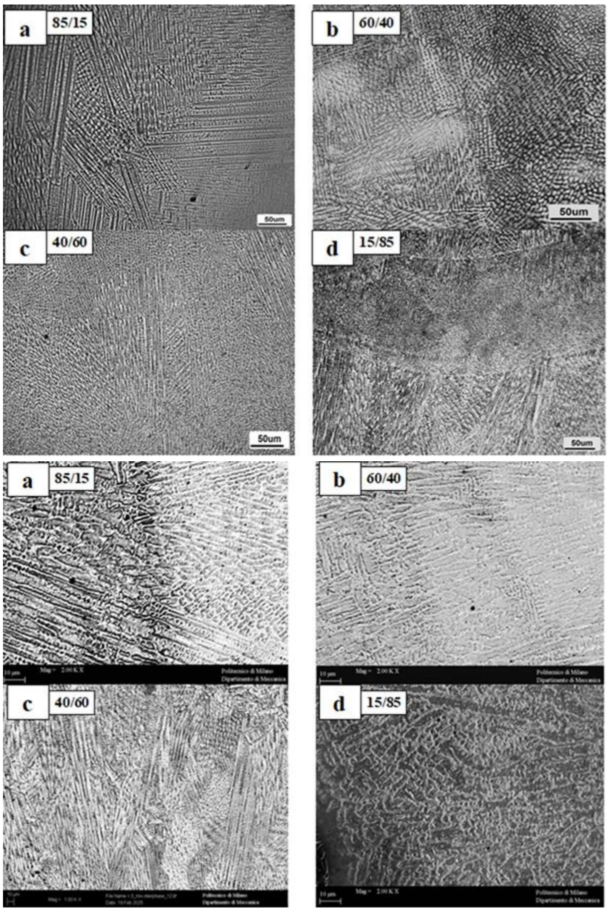

Figure 12. OM and SEM images of the composition region at different mixing ratio at v=30 mm/s.

3.2. Microhardness Test

At a linear energy density of 20 J/mm, this joining condition results in a relatively small pool of molten metal with sufficient thermal stability and rapid cooling during solidification. These conditions also reduce the distance between metal crystals and limit the diffusion time of atoms, which leads to the precipitation of Nb and Mo elements at the grain boundaries, but in the form of small, dispersed particles rather than continuous layers, while a significant portion of the alloying elements (nickel, cobalt, molybdenum, and niobium) remains dissolved in the matrix. This interplay between solid solution strengthening (nickel, cobalt, and molybdenum in the crystal lattice) and precipitation strengthening (fine particles at the grain boundaries) contributes to increased material strength without cracking. The higher IN625 fraction increases intrinsic hardness via Ni-based solid solution and precipitation strengthening, while El controls thermal input and microstructural scale-El values for the tested speeds are 30 J/mm (20 mm/s), 24 J/mm (25 mm/s), and 20 J/mm (30 mm/s).

The basic relationship of material quality in LDED is the volumetric energy density (VED) in J/mm³, mathematically expressed as [22].

$$VED = \frac{P}{v\,t\,d} \quad \text{--------------} \quad (1)$$

where P laser power (W),
v scan speed (mm/s),
d spot diameter (mm),
and t layer thickness (mm).
Nevertheless, for single-track depositions, the fixed spot size (1.2 mm) and layer thickness (0.2 mm) in each deposition track, the linear energy density, mathematically specified as [22],

$$El = \frac{P}{v} \quad \text{-------------------} \quad (2)$$

becomes the dominant parameter controlling melt pool characteristics.

Lower El (higher scan speed) reduces thermal accumulation, refines dendritic/cellular features, and raises dislocation density, producing higher hardness; conversely, higher El promotes grain/dendrite coarsening and local softening [23,24]. The measured maximum hardness therefore appears where a relatively high IN625 content (40% SS/60%) coincides with the lowest El (30 mm/s/20 J/mm), whereas combinations with excessive El or increased porosity reduce the effective load-bearing area and lower apparent microhardness. The 40%:60% ratio of 316L stainless steel to Inconel 625 alloy also improves the liquid viscosity and surface tension balance, enhancing interlayer adhesion, improving fluid flow, and reducing porosity and defects. Since the fusion depth at 20 J/mm is sufficient for complete melting without causing porosity, which avoids defects in the process. These phenomena collectively explain the reduced porosity (small gas pores instead of irregular voids) and increased density of the resulting material.

In summary, this composition (40% SS316L and 60% IN625) at a speed of 30 mm/s showed the best results in considering of hardness. The rapid solidification process enhances the crystal structure and material properties, while the stable pool of molten metal and complete melting contribute to a high-quality process, achieving an ideal balance between high strength, low porosity, and high density [25].

As shown in Fig. 13, hardness rises with increasing IN625 fraction and with higher scan speed, while porosity remains very low across all samples and is minimal at the condition combining the intermediate composition and the highest velocity. As shown in Fig. 14, a lower VED value (higher v value) with a balanced composition results in a finer microstructure and increased hardness, along with simultaneous stabilization of the melt pool, which reduces porosity and increases density. This promotes faster solidification, finer cell/dendrite spacing, and stronger solid solution/precipitate hardening, which explains the observed increase in hardness. At the same time, soluble chemical composition reduces the surface tension of the melt pool, improves wetting, and minimizes turbulence and gas entrapment, leading to lower porosity and higher density.

Lower scan speed leads to a larger ratio between the temperature gradient at the solid–liquid interface and the solidification (interface) growth rate-controlled features (coarser SDAS, segregation, Laves/intermetallics); higher scan speed leads to a higher cooling rate, so refined cellular/dendritic microstructure, less interdendritic segregation, and higher hardness [26].

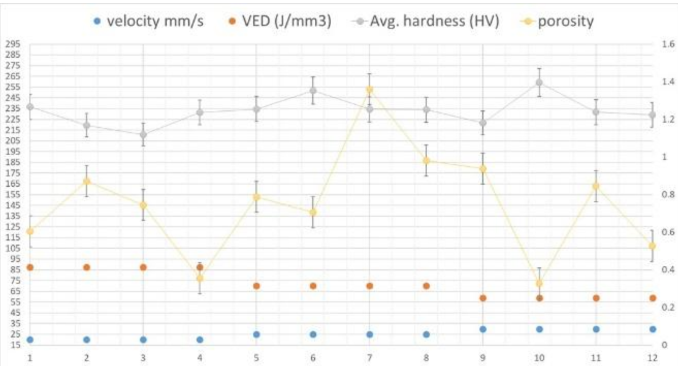

Figure 13. Relationship between velocity, VED, avg. hardness and porosity.

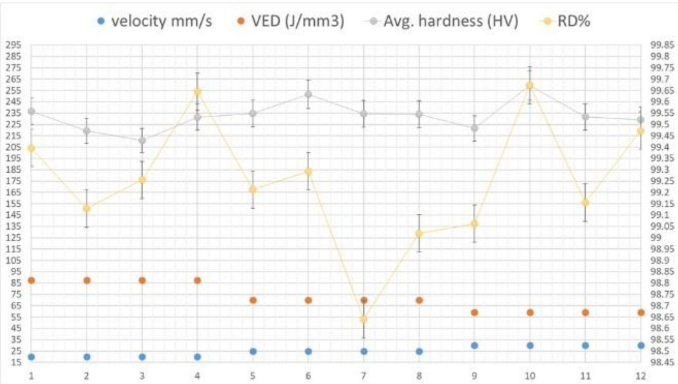

Figure 14. Relationship between velocity, avg. hardness, VED, and RD%

3.3. Porosity and relative density (RD%) Measurement

The porosity fraction and relative density (RD) were quantified from cross-sectional images acquired using a Mitutoyo optical measurement system. The images were subsequently processed in ImageJ to determine the pore area fraction, from which the relative density was calculated. The resulting values reflect the interaction between thermal input and compositional mixing during laser deposition.

In laser-directed energy deposition, the linear energy density governs the thermal energy delivered per unit length of the deposition path and therefore directly influences melt pool size, melt lifetime, and solidification conditions. At high scan speed, the melt pool becomes larger and remains liquid for longer durations, which may promote keyhole instability, vaporization, and gas entrapment within the molten metal [27]. These phenomena increase the probability of pore formation during solidification. Conversely, at very low density (high scan speed), the melt pool becomes smaller and the interaction time between the laser and powder stream decreases. Under such conditions, incomplete melting and insufficient wetting may occur, which can generate lack-of-fusion defects and irregular porosity [28]. Therefore, both excessively high and excessively low energy densities can promote porosity through different mechanisms.

Within the investigated parameter range, an intermediate linear energy density of 20 J/mm (600 W, 30 mm/s) provided the most stable thermal conditions for melt pool formation and solidification. Under this condition, the melt pool size was sufficient to ensure complete melting and wetting of the powder particles while avoiding excessive vaporization or keyhole instability. Rapid but stable solidification promoted a uniform cellular-dendritic microstructure and allowed gas bubbles to escape before being trapped in the solidifying matrix. As a result, this condition produced the highest relative density (99.673%) and the lowest measured porosity (0.327%) among the investigated samples.

Material composition also contributed to the observed densification behavior. Increasing the IN625 fraction improves melt fluidity due to the higher Ni content, which enhances melt wetting and promotes pore elimination [29]. In contrast, regions rich in SS316L tend to exhibit higher susceptibility to incomplete fusion and gas entrapment when insufficient thermal energy is supplied [30]. However, excessive IN625 fractions may also intensify segregation effects associated with Ni–Mo-rich interdendritic regions, which can destabilize melt flow and increase pore formation when combined with unsuitable energy input [31]. Consequently, the porosity and relative density observed in Figs. 15 and 16, trends arise from the combined influence of thermal input and compositional mixing.

Among the investigated conditions, the 40% SS316L–60% IN625 composition processed at 30 mm/s (20 J/mm) produced the most stable melt pool behavior and the most uniform mixing between the Fe-based and Ni-based constituents. This balanced composition improved wetting and melt fluidity while maintaining sufficient solidification stability to minimize segregation-driven porosity. As a result, this condition exhibited the most favorable densification characteristics and microstructural continuity within the graded region.

Overall, the experimental results demonstrate that porosity evolution in the SS316L–IN625 functionally graded system is controlled by the coupled effects of linear energy density, melt pool stability, and compositional dilution, which together determine solidification dynamics and gas escape behavior during deposition. Table 4 summarizes the effect of composition ratio and scanning speed (energy density) on the microhardness, porosity, and relative density of the SS316L–IN625 graded samples.

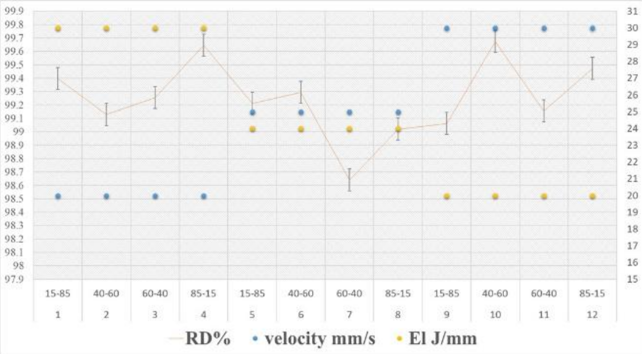

Figure 15. Relationship between composition, velocity, E_l and RD%.

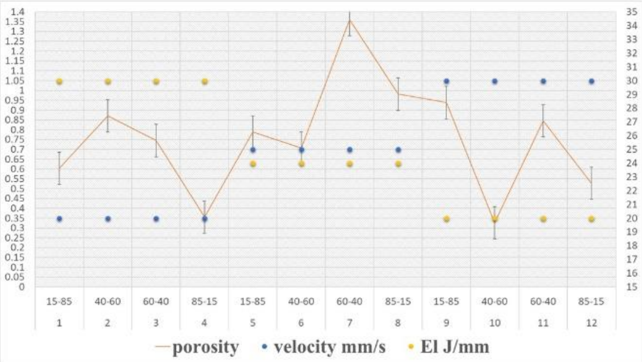

Figure 16. Relationship between composition, velocity, E_l and porosity

Table 5. Effects of energy density on the microhardness, porosity, and relative density

samples	comp.	v (mm/s)	El (J/mm)	/ED(J/mm3	Avg. (HV)	porosity	RD%
1	15-85	20	30	87.5	236.5	0.604	99.396
2	40-60	20	30	87.5	219.5	0.871	99.129
3	60-40	20	30	87.5	210.8	0.745	99.255
4	85-15	20	30	87.5	231.5	0.355	99.645
5	15-85	25	24	70	234.6	0.788	99.212
6	40-60	25	24	70	251.6	0.706	99.294
7	60-40	25	24	70	234.3	1.36	98.64
8	85-15	25	24	70	234	0.981	99.019
9	15-85	30	20	59	221.5	0.938	99.062
10	40-60	30	20	59	259.3	0.327	99.673
11	60-40	30	20	59	231.7	0.845	99.155
12	85-15	30	20	59	229	0.527	99.473

4. Conclusion

Twelve samples of Functionally graded SS316L–IN625 structures were successfully fabricated using laser-directed energy deposition under controlled compositional gradients and scanning speeds. The results demonstrate that the combined effects of linear energy density, melt-pool stability, and compositional dilution govern the evolution of microstructure, densification behavior, and mechanical response in the graded system.

Microstructural observations revealed that increasing scan speed significantly increases cooling rate, leading to progressive refinement of the cellular–dendritic solidification structure and suppression of interdendritic segregation. Under these conditions, the graded region exhibits improved metallurgical continuity and reduced defect formation. Conversely, higher thermal input promotes dendrite coarsening, segregation of Nb- and Mo-rich constituents, and increased likelihood of defect accumulation.

Quantitative porosity analysis showed that densification is strongly dependent on the interaction between thermal input and alloy composition. Among the investigated parameters, the condition corresponding to 600 W laser power and 30 mm s^{-1} scan speed (El = 20 J mm^{-1}) produced the most stable melt-pool behavior and the most favorable solidification conditions. This regime yielded the highest relative density (99.673 %) and the lowest measured porosity (0.327 %), indicating improved melt wetting, efficient gas escape during solidification, and reduced lack-of-fusion defects.

The compositional gradient also influenced mechanical performance. Increasing IN625 content enhanced hardness through combined solid-solution strengthening and fine precipitation of Nb- and Mo-rich phases, while the refined microstructure produced at higher scan speeds further increased resistance to localized plastic deformation. The highest hardness values were therefore obtained when the 40 wt.% SS316L–60 wt.% IN625 composition coincided with the lowest investigated linear energy density.

Integrating the microstructural observations, porosity measurements, relative density results, and hardness data indicates that the 40 wt.% SS316L–60 wt.% IN625 composition processed at 30 mm s^{-1} provides the most balanced condition within the studied processing window. Under these parameters, the graded region exhibits uniform cellular–dendritic morphology, minimal defect population, stable compositional transition, and enhanced mechanical response.

Overall, the study demonstrates that the performance of SS316L–IN625 functionally graded materials fabricated by LDED is governed by the coupled interaction between processing parameters, melt-pool thermodynamics, and compositional mixing, providing experimentally supported insights into the process–structure–property relationships of graded Fe–Ni alloy systems.

5.Acknowledgments

This work was supported by SITEC-Laboratory for Laser Applications, Department of Mechanical Engineering/ Politecnico di Milano, Italy, with special thanks to Akshay Ashok Benni.

6.References

[1] H. R. Zareie Rajani, S. A. A. Akbari Mousavi, and F. Madani Sani, "Comparison of corrosion behavior between fusion cladded and explosive cladded Inconel 625/plain carbon steel bimetal plates," Mater. Des., vol. 43, pp. 467-474, 2013. https://doi.org/10.1016/j.matdes.2012.06.053

[2] K. Shah, A. Pinkerton, L. Li, and J. McGourlay, "Parametric study of development of Inconel-steel functionally graded materials by laser direct metal deposition," Mater. Des., vol. 54, pp. 531-538, 2014. https://doi.org/10.1016/j.matdes.2013.08.079

[3] W. J. Sames, F. A. List, S. Pannala, R. R. Dehoff, and S. S. Babu, "The metallurgy and processing science of metal additive manufacturing," Int. Mater. Rev., vol. 61, no. 5, pp. 315-344, 2016. https://doi.org/10.1080/09506608.2015.1116649

[4] W. Li, Y. Li, Z. Li, C. Zhang, and Y. Huang, "Fabrication and characterization of a functionally graded material from Ti-6Al-4V to SS316 by laser metal deposition," Addit. Manuf., vol. 14, pp. 95-104, 2017. https://doi.org/10.1016/j.addma.2016.12.006

[5] B. E. Carroll, R. R. Dehoff, S. L. Babu, and S. Pannala, "Functionally graded material of 304L stainless steel and Inconel 625 fabricated by directed energy deposition:

Characterization and thermodynamic modeling," Acta Mater., vol. 108, pp. 46-54, 2016. https://doi.org/10.1016/j.actamat.2016.02.019

[6] R. Ghanavati, H. Naffakh-Moosavy, M. Moradi, and M. Eshraghi, "Printability and microstructure of directed energy deposited SS316L-IN718 multi-material: Numerical modeling and experimental analysis," Sci. Rep., vol. 12, p. 16600, 2022. https://doi.org/10.1038/s41598-022-21077-8

[7] A. Bandyopadhyay and B. Heer, "Additive manufacturing of multi-material structures," Mater. Sci. Eng. R Rep., vol. 129, pp. 1-16, 2018. https://doi.org/10.1016/j.mser.2018.04.001

[8] S. Hasanov, S. Alkunte, M. Rajeshirke, A. Gupta, O. Huseynov, I. Fidan, F. Alifui-Segbaya, and A. Rennie, "Review on additive manufacturing of multi-material parts: Progress and challenges," J. Manuf. Mater. Process., vol. 6, no. 4, 2022. https://doi.org/10.3390/jmmp6010004

[9] C. Zhong, J. Kittel, A. Gasser, and J. H. Schleifenbaum, "Study of nickel-based super-alloys Inconel 718 and Inconel 625 in high-deposition-rate laser metal deposition," Opt. Laser Technol., vol. 109, pp. 352-360, 2019. https://doi.org/10.1016/j.optlastec.2018.08.003

[10] B. Chen, Y. Zhang, H. Zhang, X. Zhang, and Y. Huang, "Development and characterization of 316L/Inconel 625 functionally graded material fabricated by laser direct metal deposition," Opt. Laser Technol., vol. 123, Art. 105916, 2019. https://doi.org/10.1016/j.optlastec.2019.105916

[11] A. A. Ferreira, J. P. Oliveira, A. M. P. Jesus, and F. M. Braz Fernandes, "Inconel 625/AISI 413 stainless steel functionally graded material produced by direct laser deposition," Materials, vol. 14, 2021. https://doi.org/10.3390/ma14195595

[12] R. Ghanavati, H. Naffakh-Moosavy, and M. Moradi, "Additive manufacturing of thin-walled SS316L-IN718 functionally graded materials by direct laser metal deposition," J. Mater. Res. Technol., vol. 15, pp. 2673-2685, 2021. https://doi.org/10.1016/j.jmrt.2021.09.061

[13] N. F. Jones, J. L. Beuth, and M. P. Boer, "Directed energy deposition joining of Inconel 625 to 304 stainless steel with direct bonding," J. Mater. Res., vol. 36, no. 23, pp. 5213-5225, 2021. https://doi.org/10.1557/s43578-021-00304-4

[14] H. Hotz, M. Schmidt, A. Gasser, and J. H. Schleifenbaum, "Additive manufacturing of functionally graded Ti-Al structures by laser-based direct energy deposition," J. Manuf. Process., vol. 68, pp. 1524-1534, 2021. https://doi.org/10.1016/j.jmapro.2021.06.068

[15] R. Gotoh, K. Takahashi, T. Balamurugesan, and Y. Kondo, "Experimental and analytical investigations of AlSi10Mg, stainless steel, Inconel 625 and Ti-6Al-4V porous materials printed via powder bed fusion," Prog. Addit. Manuf., vol. 7, pp. 943-955, 2022. https://doi.org/10.1007/s40964-022-00269-8

[16] G. Jiang, Y. Zhang, H. Wang, X. Li, and C. Liu, "Effect of dissolved precursors on corrosion characteristics of Ni-based alloy Inconel 625, stainless steel 316L and titanium alloy TA2 in acidic and neutral supercritical water: A comparative study," J. Supercrit. Fluids, vol. 209, Art. 106249, 2024. https://doi.org/10.1016/j.supflu.2024.106249

[17] N. Chen, X. Zhang, Y. Li, and H. Wang, "Microstructural characteristics and crack formation in additively manufactured bimetal material of 316L stainless steel and Inconel 625," Addit. Manuf., vol. 32, Art. 101037, 2020. https://doi.org/10.1016/j.addma.2020.101037

[18] S. K. Gürel, İ. A. Yüksel, and T. O. Kılınç, "Uncertainty calculations and calibration of metal hardness testing equipment," 19th Int. Congr. Metrol., Art. 12002, 2019. https://doi.org/10.1051/metrology/201912002

[19] D. D. Singh, S. Arjula, and A. R. Reddy, "Influence of laser power on mechanical properties of FGM of SS316L and IN625 fabricated by direct metal deposition," E3S Web Conf., vol. 552, Art. 01016, 2024. https://doi.org/10.1051/e3sconf/202455201016

[20] X. Xu, G. Mi, Y. Luo, P. Jiang, X. Shao, and C. Wang, "Morphologies, microstructures, and mechanical properties of samples produced using laser metal deposition with 316L stainless steel wire," Opt. Lasers Eng., vol. 94, pp. 1-11, 2017. https://doi.org/10.1016/j.optlaseng.2017.02.008

[21] Q. Y. Jin, Y. Li, Z. Zhang, H. Wang, and C. Liu, "Design of dissimilar material joint for defect-free multi-material additive manufacturing via laser-directed energy deposition," Heliyon, vol. 10, no. 15, Art. e29666, 2024. https://doi.org/10.1016/j.heliyon.2024.e29666

[22] G. Gong, J. Ye, Y. Chi, Z. Zhao, Z. Wang, G. Xia, X. Du, H. Tian, H. Yu, and C. Chen, "Research status of laser additive manufacturing for metal: A review," J. Mater. Res. Technol., vol. 15, pp. 855-884, 2021. https://doi.org/10.1016/j.jmrt.2021.08.050

[23] J. K. Chaurasia, S. K. Singh, A. Kumar, and R. K. Singh, "Effect of deposition strategy and post-processing on microstructure and mechanical properties of serviced Inconel 625 parts repaired using laser directed energy deposition," Opt. Laser Technol., vol. 168, Art. 109831, 2024. https://doi.org/10.1016/j.optlastec.2023.109831

[24] Z. Liu, Y. Li, H. Wang, and C. Liu, "Directed energy deposition of functional gradient material to enhance mechanical properties of heterogeneous stainless steels," Opt. Laser Technol., vol. 179, Art. 111326, 2024. https://doi.org/10.1016/j.optlastec.2024.111326

[25] M. G. Mouziraji, A. M. Al-Hussein, S. Al-Quraishi, and H. Al-Jubouri, "A review study on metal powder materials and processing parameters in laser metal deposition," Opt. Laser Technol., vol. 170, Art. 110226, 2024. https://doi.org/10.1016/j.optlastec.2023.110226

[26] X. Tong, Y. Li, Z. Zhang, H. Wang, and C. Liu, "Microstructures and mechanical properties of crack-free 316L stainless steel and Inconel 625 joint by using Laser Engineered Net Shaping," Opt. Laser Technol., vol. 155, Art. 108357, 2022. https://doi.org/10.1016/j.optlastec.2022.108357

[27] Y. Liu, Z. Zhang, H. Wang, and C. Liu, "Heterogeneous microstructure and tensile properties of HA188/SS316L functionally graded materials prepared by laser directed energy deposition," Opt. Laser Technol., vol. 181, Art. 111770, 2025. https://doi.org/10.1016/j.optlastec.2024.111770

[28] A. K. Praharaj, S. K. Singh, R. K. Singh, and J. K. Chaurasia, "Enhanced tribological performance of laser directed energy deposited Inconel 625 achieved through laser surface remelting," Surf. Coatings Technol., vol. 477, Art. 130345, 2024. https://doi.org/10.1016/j.surfcoat.2023.130345

[29] M. H. Nie, Y. Li, Z. Zhang, H. Wang, and C. Liu, "Studies on the 316/NiTi functionally gradient ultra-thick coatings fabricated with directed energy deposition: Microstructure, crystallography and wear mechanism," Appl. Surf. Sci., vol. 630, Art. 157497, 2023. https://doi.org/10.1016/j.apsusc.2023.157497

[30] R. Zhang, Y. Li, Z. Zhang, H. Wang, and C. Liu, "Molten pool swing in printing the steel/Inconel functionally gradient material with laser-based directed energy deposition," Manuf. Lett., vol. 32, pp. 44-48, 2022. https://doi.org/10.1016/j.mfglet.2022.03.002

[31] K. Li, Y. Li, Z. Zhang, H. Wang, and C. Liu, "A functionally graded material design from stainless steel to Ni-based superalloy by laser metal deposition coupled with thermodynamic prediction," Mater. Des., vol. 217, Art. 110612, 2022. https://doi.org/10.1016/j.matdes.2022.110612